Journal of Fluids and Structures (2000) **14,** 757–777
doi:10.1006/jfls.2000.0297, available online at http://www.idealibrary.com on IDEAL®

SIMULATION OF THE FLOW OVER ELLIPTIC AIRFOILS OSCILLATING AT LARGE ANGLES OF ATTACK

M. H. Akbari and S. J. Price

Department of Mechanical Engineering, McGill University
Montréal, Québec, Canada H3A 2K6

(Received 19 November 1999)

The incompressible, viscous flow over two-dimensional elliptic airfoils oscillating in pitch at large angles of attack, such that flow separation occurs, has been simulated numerically for a Reynolds number of 3000. A vortex method is used to solve the two-dimensional Navier–Stokes equations in vorticity/stream-function form using a time-marching approach. Using an operator-splitting method the convection and diffusion equations are solved sequentially at each time step. The convection equation is solved using a vortex-in-cell method, and the diffusion equation using a second-order ADI finite-difference scheme. Elliptic profiles are obtained by mapping a circle in a computational domain into the physical domain using a Joukowski transformation. The effects of several parameters on the flow field are considered, such as: frequency of oscillation, mean angle of attack, location of pitch-axis and the thickness ratio of the ellipse. The results obtained are shown to compare favourably with available experimental results.

1. INTRODUCTION

An elliptic geometry represents a general configuration allowing the realization of a wide range of cross-sections, from a circular cylinder to a flat plate. Depending on the thickness ratio and the angle of attack of the ellipse, its flow field may show some characteristics of bluff-body flow, such as a circular cylinder in cross-flow, or those of the flow over a streamlined body, such as an airfoil. At low angles of attack the flow over slim elliptic cylinders generally remains attached to the body surface, and the ellipse behaves in a similar manner to a conventional airfoil. On the other hand, at high angles of attack, or for ellipses with high thickness ratios, the flow separates from a considerable portion of the surface, and a bluff-body flow regime is observed.

The study of elliptic cylinders in cross-flow has been the subject of several numerical and experimental investigations. For example, using a finite-difference scheme, Lugt & Haussling (1974) studied the impulsively started flow over an elliptic cylinder. A 10% thick elliptic cylinder at $\mathrm{Re} = 200$ was considered with an angle of attack of 45°, where the ellipse behaved as a bluff body. A separated flow regime, along with periodic vortex shedding from the ellipse was observed, producing a Kármán vortex street in the wake. Chou & Huang (1996) also studied the impulsively started unsteady flow around elliptic cylinders with different thickness ratios at very high angles of attack ($\alpha = 60°, 90°$), and at Reynolds numbers of up to 1000. They used a semi-implicit finite-difference scheme to solve the Navier–Stokes equations in terms of vorticity and stream-function. For a 10% thick ellipse at $\alpha = 90°$ and $\mathrm{Re} = 1000$ the formation of a secondary eddy, as usually obtained for a circular cylinder in cross-flow, was *not* observed during the early stages of the flow. They

0889–9746/00/080757 + 21 $35.00/0

reported that the growth of the main eddy was much faster than that behind a circular cylinder. Mittal & Balachandar (1996) developed a spectral collocation technique to simulate the three-dimensional incompressible flow over elliptic cylinders in the Reynolds number range of 180–1000. They observed that, in general, the 2-D simulations predicted a higher mean drag compared to the corresponding 3-D simulations. However, they reported that for Reynolds numbers where the flow is known to be intrinsically three-dimensional the 2-D simulations estimated the drag more accurately for streamlined bodies than for bluff bodies.

Nair & Sengupta (1996) numerically investigated the onset of asymmetry over elliptic cylinders, with different thickness ratios, in an impulsively started flow at a Reynolds number of 10^4. They used a finite-difference scheme to solve the Navier–Stokes equations in the stream-function/vorticity form. The asymmetry started to develop at earlier times for the ellipses compared to a circular cylinder. However, the asymmetry developed at a faster rate for a thicker ellipse. They linked the onset of asymmetry around an object to the streamline curvature near the trailing edge. Nair & Sengupta (1997) also investigated the *early stages* of a two-dimensional flow past elliptic cylinders at constant angles of attack. For a 10% thick ellipse, at $\mathrm{Re} = 3000$ and $\alpha = 30^\circ$, a very vortical and separated flow structure was predicted shortly after the impulsive start of the flow. For angles of attack of $\alpha = 10$ and 12°, separated flows were also predicted over the same ellipse, although the flow separated at later times compared to the case with $\alpha = 30^\circ$. It was noted that for the 10% thick elliptic cylinder the flow field behaved very much like that over a conventional airfoil

A number of experimental investigations of the flow over elliptic cylinders have also been performed. For example, Modi & Wiland (1970) studied the fluctuating loading and vortex shedding frequency, and Modi & Dikshit (1975) studied the near-wake aerodynamics and wake geometry for static elliptic cylinders as a function of thickness ratio and angle of attack in the subcritical Reynolds number range. Surface pressure measurements were reported by Ota *et al.* (1985) for an elliptic cylinder of axis ratio 1 : 3 in the critical Reynolds number range.

Ohmi *et al.* (1990) used both flow visualization and numerical calculations to study the *early stages* of an impulsively started flow, with $\mathrm{Re} = 1500$ to 10^4, over a 10% thick, pitching elliptic cylinder. It was observed that the dominant parameter affecting the results was the reduced frequency of oscillation $f^* \equiv fc/U_\infty$ (where f, c, and U_∞ are the frequency of oscillation, the chord length, and the upstream velocity, respectively). For $f^* = 0{\cdot}2$, and a mean angle of attack $\bar{\alpha} = 30^\circ$, they observed that the starting flow retained the fundamental characteristics of static stall over a fixed airfoil. At this reduced frequency the rotational motion of the airfoil produced only secondary effects on the vortex development in the wake. At higher reduced frequencies of 1·0 or 2·0, on the other hand, the vortex formation was primarily due to the fluid reaction to the transverse motion of the leading- and trailing-edges of the ellipse. The effect of the Reynolds number was found to be much less important than that of other parameters.

In this paper the early stages of flow development over elliptic airfoils is simulated, and the effects of several airfoil parameters on the flow field are investigated.

2. SOLUTION METHOD

The governing equations for the incompressible flow of a Newtonian fluid are the Navier–Stokes and continuity equations, which for a two-dimensional flow can be

expressed in terms of the vorticity and stream-function as follows:

$$\frac{\partial \omega}{\partial t} + (\mathbf{u} \cdot \nabla)\omega = \nu \nabla^2 \omega, \tag{1}$$

$$\nabla^2 \psi = -\omega, \tag{2}$$

where $\mathbf{u} = (u, v)$ is the velocity vector, ν is the kinematic viscosity, and ω and ψ are the vorticity and stream-function, respectively. Equation (2) is the Poisson equation for the stream-function, which replaces the continuity equation.

In this study an elliptic cylinder oscillating in the pitch direction is considered, such that the instantaneous angle of attack, α, is given by

$$\alpha = \bar{\alpha} + A\cos(\Omega t), \tag{3}$$

where $\bar{\alpha}$ is the mean angle of attack, A is the amplitude of the pitching oscillation (in rad), and $\Omega = 2\pi f$, with f being the frequency of oscillation.

Following Chorin (1973), an "operator-splitting" method is applied to the governing equations, and the following two equations are obtained, which are solved sequentially at each time step:

$$\frac{\partial \omega}{\partial t} = -(\mathbf{u} \cdot \nabla)\omega, \tag{4}$$

$$\frac{\partial \omega}{\partial t} = \nu \nabla^2 \omega. \tag{5}$$

Convergence proofs for the application of the operator-splitting method to the Navier–Stokes equations for unbounded flows are given by Beale & Majda (1981) and Ying (1990).

The vorticity field is discretized into a number of point vortices, and the time domain is also discretized into small time steps. Equation (4) states that the total derivative of vorticity is zero during "convection", or that the vorticity of a particle is constant as it is convected with the local velocity. Hence, in order to satisfy the "convection" part of the governing equations, the velocity field is obtained, and each "vortex particle" is convected with the local velocity for the short period of the time step. To determine the velocity field equation (2) is solved for the stream-function (given the vorticity field), and the velocity field is then computed as the curl of the stream function. Next, the diffusion process is simulated by solving equation (5) using a second-order ADI finite difference scheme. The "no-flow" boundary condition is satisfied during the solution of the convection problem, and the "no-slip" boundary condition is satisfied by the creation of new vorticity on the body surface during each time-step.

The boundary condition on the surface of the body is expressed as

$$\mathbf{u} = \mathbf{v}_b \quad \text{on the surface of the pitching body},$$

where $\mathbf{u} = (u, v)$ is the velocity of the fluid adjacent to the body surface, and $\mathbf{v}_b$ is the local velocity vector of the surface of the body. The velocity $\mathbf{v}_b$ is given, at any point w on the surface, by

$$\mathbf{v}_b = \dot{\boldsymbol{\alpha}} \times (\mathbf{w} - \mathbf{P}), \tag{6}$$

where $(\mathbf{w} - \mathbf{P})$ is a "position vector" from the axis of rotation (P) to the point under consideration (w), and $\dot{\boldsymbol{\alpha}}$ is the angular velocity vector, which, in this case, is perpendicular

to the 2-D physical plane. The magnitude of the angular velocity is given by

$$\dot{\alpha} = -A\,\Omega \sin(\Omega t). \tag{7}$$

2.1. Solution of the Convection Equation

The velocity field is calculated by first solving the Poisson equation for the stream-function through the so-called "vortex-in-cell" method, and then taking the curl of this computed stream-function. Examples of the application of this scheme can be found in Smith & Stansby (1988), Meneghini & Bearman (1993) and Akbari & Price (1997). In order to more readily solve the Poisson equation, a conformal transformation is used to map a circle in a **z**-plane onto an ellipse in a **w**-plane, with $\mathscr{F}: \mathbf{z}(x, y) \rightarrow \mathbf{w}(\xi, \eta)$. The Poisson equation is then solved in the circle- or **z**-plane, rather than in the physical domain (**w**-plane).

The general form of this transformation is given by

$$w = \mathscr{F}(z) = \left[\left(z + \frac{(C-B)^2}{z}\right) - P\right] e^{-i\alpha} + P, \tag{8}$$

where $z = x + i\,y$ is a point on or outside the circle in the **z**-plane, $w = \xi + i\eta$ is the corresponding point on or outside the transformed profile in the **w**-plane, B is a control parameter to be explained later, and C, α and P are described below with the help of Figure 1.

As can be seen in Figure 1, C is the location of the intersection of the circle in the **z**-plane with the positive side of the x-axis. The center of the circle is located at the point $(-\varepsilon, \delta)$, P is the location of the axis of rotation of the profile in the **w**-plane, and α is the angle of rotation (angle of attack), positive in the clockwise direction. As mentioned above, B is a control parameter that, along with the eccentricity of the circle, determines the shape of the profile in the transformed plane (**w**-plane). Giving an eccentricity to the circle results in a Joukowski airfoil. However, throughout the present study we set

$$\varepsilon = \delta = 0,$$

to obtain an elliptic profile in the transformed plane. In order to get different values of thickness ratio for the ellipse, the value of parameter B is changed.

Given equation (8), one can easily obtain $\mathscr{F}'(z)$, defined as $\mathscr{F}'(z) \equiv \mathrm{d}\mathscr{F}(z)/\mathrm{d}z = \xi_x + i\,\eta_x$ (where ξ_x and η_x are the metrics of the transformation). Thus, the Jacobian $\mathscr{J}$ of the transformation may be obtained easily, since the transformation is analytical, and hence,

$$\mathscr{J} = \xi_x^2 + \eta_x^2 = |\mathscr{F}'(z)|^2. \tag{9}$$

This Jacobian is necessary in the solution procedure, as discussed in the following.

Because the Poisson equation is solved in the circle–plane, correct boundary conditions are required in this plane. Hence, a correspondence to equation (6) is required in the **z**-plane (circle-plane). Given $w = \mathscr{F}(z)$, and using the chain rule, it can be shown that

$$\dot{w} = \mathscr{F}'(z)\,\dot{z}, \tag{10}$$

where $\dot{w}$ and $\dot{z}$ are, respectively, complex velocities in the **w**- and **z**-plane, corresponding to each other, and defined as

$$\dot{w} = u + iv, \quad \dot{z} = \hat{u} + i\hat{v}.$$

Equation (6) enables $\dot{w}$ to be determined on the surface, then using equation (10) and the above definitions, the velocity components $\hat{u}$ and $\hat{v}$ in the **z**-plane can be obtained. Given

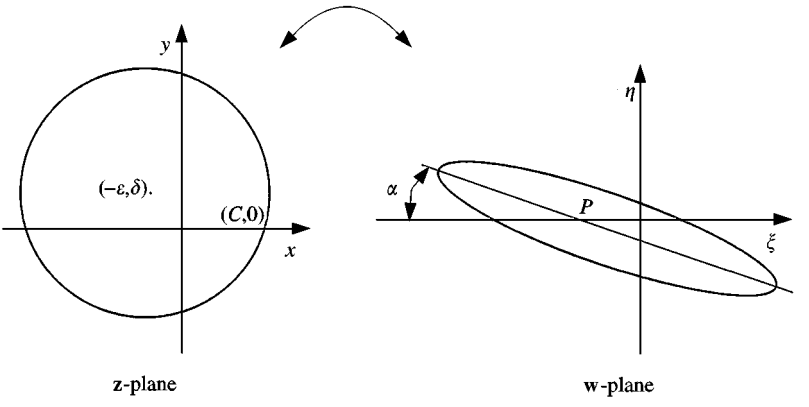

Figure 1. The Joukowski transformation of the **z**-plane (circle) into the **w**-plane (ellipse).

$\hat{u}$ and $\hat{v}$, the following equations are integrated to obtain the boundary conditions for the stream-function on the circle in the **z**-plane:

$$\hat{u} = \frac{1}{\mathscr{J}}\frac{\partial \psi}{\partial y}, \quad \hat{v} = -\frac{1}{\mathscr{J}}\frac{\partial \psi}{\partial x}. \tag{11,12}$$

This integration is conducted along the body surface, starting from an arbitrary reference point (e.g. the trailing-edge); thus, the inner boundary condition of the stream-function for the solution of the Poisson equation is obtained.

The outer boundary condition of the stream-function is obtained as follows. If the outer edge of the grid mesh is set far enough from the body, then it is reasonable to assume that the flow field is not altered there by the presence of the body, and hence

$$\begin{cases} u = U_\infty \\ v = 0 \end{cases} \quad \text{at the far field,}$$

or

$$\dot{w} = U_\infty \quad \text{at the far field.} \tag{13}$$

On the other hand, from equation (8), one can easily arrive at

$$\lim_{z \to \infty} \mathscr{F}'(z) = \mathrm{e}^{-\mathrm{i}\alpha}, \tag{14}$$

and using equation (10) gives

$$\lim_{z \to \infty} \dot{z} = U_\infty \mathrm{e}^{\mathrm{i}\alpha} = U_\infty(\cos\alpha + \mathrm{i}\sin\alpha), \tag{15}$$

and hence

$$\begin{cases} \hat{u} = U_\infty \cos\alpha \\ \hat{v} = U_\infty \sin\alpha \end{cases} \quad \text{at the far field.} \tag{16}$$

Then, since

$$\lim_{z \to \infty} \mathscr{J} = \lim_{z \to \infty} |\mathscr{F}'(z)|^2 = 1,$$

and using equations (11), (12), and (16), one can easily arrive at the following for the outer boundary condition of the stream-function:

$$\psi = U_\infty(y\cos\alpha - x\sin\alpha) + \text{const.} \qquad \text{at the far field.} \tag{17}$$

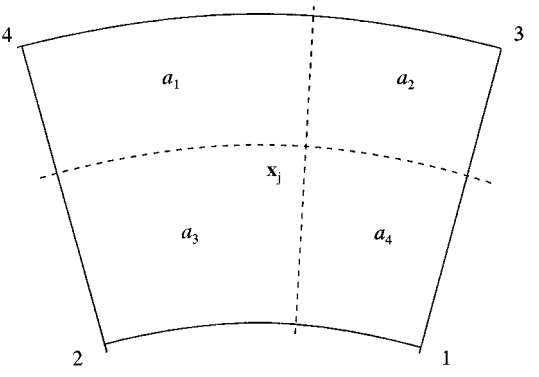

Figure 2. A typical polar cell containing a vortex.

A polar grid is set up in the **z**-plane concentric with the circular boundary. The grid is uniform in the circumferential direction and exponentially expanding in the radial direction. Figure 2 shows a typical cell of such a grid, which in this case contains the jth point vortex with strength Γ_j located at $\mathbf{x}_j$. The ray and the arc (concentric with the grid) that pass through $\mathbf{x}_j$ cut the cell into four segments. The surface areas of these segments are denoted as $a_i, i = 1, \ldots, 4$, such that a_i corresponds to the segment on the opposite side of corner i, as shown in the Figure 2.

The vorticity due to the jth vortex is now distributed onto the four surrounding nodes as follows:

$$\omega_i = \frac{a_i}{(a_{\text{total}})^2}\Gamma_j, \quad i = 1, \ldots, 4, \tag{18}$$

where a_{total} is the total area of the cell. Note that a uniform distribution of vorticity $(\Gamma_j/a_{\text{total}})$ over the cell due to the jth vortex has been assumed. All other vortices are interpolated onto the grid in a similar manner, and, due to the linearity of the problem, the total vorticity at a node is simply the sum of the contributions from the individual vortices.

In the present analytical scheme, which involves the transformation of the physical boundary onto a circle, the surface areas of the cell segments should be modified as follows:

$$a_i' = a_i \mathscr{J}(\bar{\mathbf{x}}_i), \quad i = 1, \ldots, 4, \tag{19}$$

where a_i' is the "corrected" surface area, a_i is the surface area of the segment in the transformed (circle) plane, and $\bar{\mathbf{x}}_i$ is the location of the centroid of the ith segment.

Now, given this discretized vorticity field and the boundary conditions of the stream-function on both the inner and outer edges of the mesh, the Poisson equation can be solved in the **z**-plane (circle-plane). Details of the fast Poisson solution scheme used in this study (the cyclic reduction method) are given by Swarztrauber & Sweet (1975), and for the sake of brevity are not presented here.

Given the stream-function, the velocity field **u** is calculated, and the vortex positions are updated as

$$\mathbf{x}_j^{k+1} = \mathbf{x}_j^k + \mathbf{u}(\mathbf{x}_j^k, t_k)\Delta t \tag{20}$$

where $\mathbf{x}_j^k$ is the position of the jth vortex at time t_k, and $\mathbf{x}_j^{k+1}$ is its position at time t_{k+1} due to the "convection" part of the problem.

2.2. The No-slip Boundary Condition

The no-slip boundary condition is satisfied by creating vortices at the solid boundary, such that the velocity field induced by these vortices cancels the tangential component of velocity along the boundary.

At the beginning of a time step the velocity field is calculated through the vortex-in-cell method, as explained in the previous section. (Note that the effect of viscosity is not considered during this velocity field calculation.) Thus, the tangential velocity component along the body surface is obtained. If the velocity component long the surface at node i is u_{τ_i}, and the length of the ith panel on the surface by s_i, a number of vortices with a total circulation (strength) of

$$(\Gamma_i)_{\text{total}} = -u_{\tau_i} s_i \tag{21}$$

is created on panel i in order to cancel out the tangential velocity, u_{τ_i}. This imitates the physical process of vorticity generation on a solid boundary in a viscous flow. The total circulation $(\Gamma_i)_{\text{total}}$ is divided equally between n point vortices located at node i, such that the strength of each of them, Γ_j, does not exceed a given maximum value, $\Gamma_{\max}$. This increases the number of vortices in the flow, resulting in a smoother vorticity field.

Note that although the new vortices are created on the surface, they will be "pushed" into the interior of the flow field through the action of diffusion. (Ideally, after the creation of new vorticity on the body surface the velocity there will vanish, thus "convection" will have no contribution in this "push".)

After the creation of new vorticity the velocity field is once again calculated for the purpose of "convecting" the vorticity field. Hence, during the "convection" stage of the solution procedure both the no-slip and the no-flow boundary conditions are satisfied. In the next time-step, the vortex positions and strengths will change due to "convection" and "diffusion", and thus, in general, the tangential velocity on the solid boundary will no longer be zero. Therefore, the same process is repeated, and new vorticity is created.

2.3. Solution of the Diffusion Equation

To solve the diffusion equation it is first transformed into the **z**-plane (circle-plane). The vorticity is then distributed onto the same grid as that used for the solution of the Poisson equation, using the same bilinear interpolation scheme. An alternating-direction-implicit (ADI) finite-difference scheme is used to solve the transformed diffusion equation. A detailed description of this scheme can be found in Akbari (1999), and for the sake of brevity is not given here.

Obviously, the nodal vorticity distributions before and after the solution of the diffusion equation are different. The nodal vorticity distribution after the diffusion process has to be interpolated back onto the point vortices in the field. Suppose that, during the distribution of the vorticity onto the grid, the jth vortex contributed an amount of vorticity to node p given by

$$\varpi_j^{p,k} = \frac{a'_p}{(a'^2_{\text{total}})_j} \Gamma_j^k, \tag{22}$$

where Γ_j^k is the strength of the jth vortex before the diffusion process (at time t_k), a'_p is the corrected surface area of the segment (of the cell) that corresponds to node p, and $(a'_{\text{total}})_j$ is the total corrected surface area of the cell containing the jth vortex. Also suppose that at the end of the vorticity distribution the total vorticity at node p is ω_p^k. Now, if after solving the

diffusion equation (at time t_{k+1}) the vorticity at node p is ω_p^{k+1}, then the contribution to the jth vortex from node p is

$$\varpi_j^{p,k+1} = \frac{\omega_p^{k+1}}{\omega_p^k} \varpi_j^{p,k}. \tag{23}$$

This is the contribution to the jth vortex from node p only. The total *strength* of this vortex after the diffusion process will be the sum of its contributions from all four surrounding nodes,

$$\Gamma_j^{k+1} = \left(\sum_{n=1}^{4} \varpi_j^{n,k+1} \right) (a'_{\text{total}})_j. \tag{24}$$

After distributing the nodal vorticity among the existing vortices, if any node still has any remaining vorticity, new vortices are created at that node with the total strength of

$$\Gamma_{\text{total}} = \frac{(\omega_p^{k+1})_{\text{leftover}}}{\overline{a'_{\text{total}}}}, \tag{25}$$

where, $(\omega_p^{k+1})_{\text{leftover}}$ is the amount of the remaining vorticity at node p, and $\bar{a}'_{\text{total}}$ is the average corrected surface area of the four surrounding cells. The condition $|\Gamma_j| \leq \Gamma_{\max}$ applies here in the same manner as applied to the solution of the convection equation, thus, if $|\Gamma_{\text{total}}| > \Gamma_{\max}$ more than one vortex is created.

3. FORCE CALCULATION

The total fluid force on a body is due to the pressure and shear stress distributions on its surface. The pressure is calculated by integrating along θ-constant curves in the **z**-plane (or along the corresponding path in the **w**-plane) starting from the outer edge of the grid, where the pressure is assumed to be zero, to the surface of the body.

Along a θ-constant curve, we have

$$\mathrm{d}p = \frac{\partial p}{\partial r} \mathrm{d}r \Big|_{\theta - \text{const.}}. \tag{26}$$

The term $\partial p/\partial r$ is obtained from the Navier–Stokes equations, as discussed by Akbari (1999).

The shear stress on a solid boundary in a Newtonian fluid is given by

$$\tau = -\mu \frac{\partial u_t}{\partial n},$$

where τ is the shear stress, μ is the dynamic viscosity, u_t is the velocity component tangent to the surface, and n is the normal direction to the surface. The term $\partial u_t/\partial n$ is transformed using the transformation $\mathscr{E}$: $\mathbf{w} \to \mathbf{z}$, to give

$$\frac{\partial u_t}{\partial n} \to \frac{\partial \hat{u}_\theta}{\partial r}. \tag{27}$$

Hence, the shear stress at any point on the body surface is given by

$$\tau = -\mu \frac{\partial \hat{u}_\theta}{\partial r}. \tag{28}$$

A finite-difference scheme is used to approximate the above equation.

Given the pressure and shear stress distributions, the lift and drag forces, F_l and F_d, can easily be obtained, and expressed in nondimensional forms as $C_l = F_l/(\frac{1}{2}\rho U_\infty^2 c)$ and $C_d = F_d/(\frac{1}{2}\rho U_\infty^2 c)$, where, U_∞ is the free-stream velocity, ρ is the fluid density, and c is the chord length of the body, which in the case of an ellipse is the length of its major axis.

4. RESULTS AND DISCUSSION

The *starting flow* over pitching ellipses is studied for Re = 3000, and the effects of some parameters on the flow field are investigated. The boundary layer and the wake of the airfoil are not considered to be turbulent at this Reynolds number [e.g. Ohmi *et al.* (1990)]. In all the simulations presented a time-step of $\Delta t = 0{\cdot}01$, and a 300×300 grid are used. It was checked that numerical convergence was achieved using these parameters. For example, using a finer grid of 400×400 resulted in a very similar time variation of force coefficients, with only a 4% difference from that obtained using the 300×300 grid. Also, decreasing the time-step to $\Delta t = 0{\cdot}0075$ had virtually no effect on the flow field or the force coefficients.

To demonstrate the accuracy of the present numerical scheme, the flow over a *stationary* ellipse with $t/c = 0{\cdot}1$ at different angles of attack is considered. The simulation results for a fixed ellipse at $\bar{\alpha} = 10^\circ$ are shown in Figure 3 in terms of vorticity contours. In this and all similar figures, positive vorticity is shown in white and negative vorticity in black, the gray areas represents (almost) zero vorticity.

As seen in Figure 3, the flow remains attached to the surface over most of the upper surface and the entire lower surface of the ellipse. The release of the starting vortex occurs during $t^* \equiv tU_\infty/c \leq 1{\cdot}5$, as shown in Figure 3(a,b) (where here t is time in seconds, and t^* is the dimensionless time). Then, a tiny separation-reattachment bubble is formed periodically at the trailing-edge, that leads to the formation and release of counter-rotating vortices from

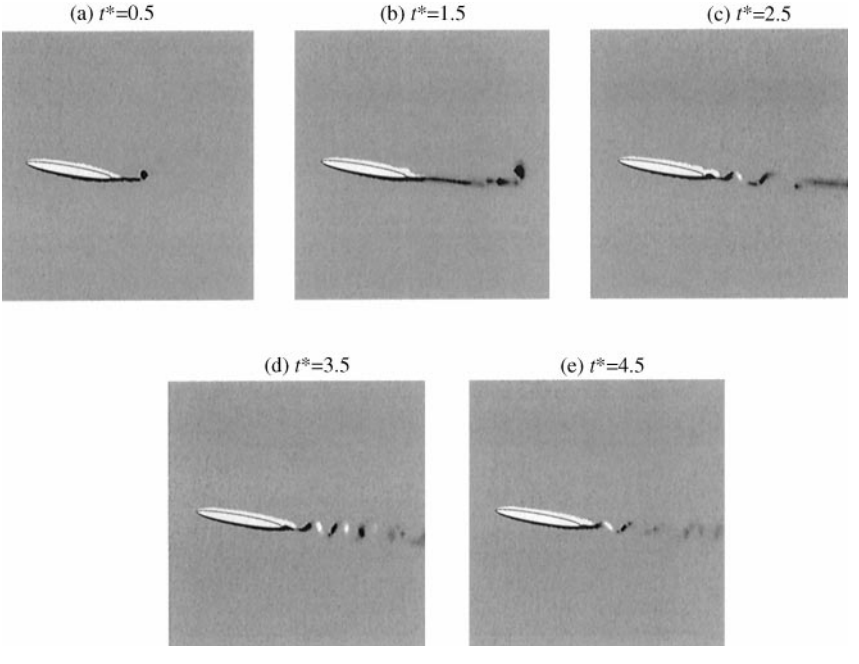

Figure 3. Vorticity contour plots at several instants of time for a fixed elliptic cylinder; $t/c = 0{\cdot}1$, $\bar{\alpha} = 10^\circ$ and Re = 3000.

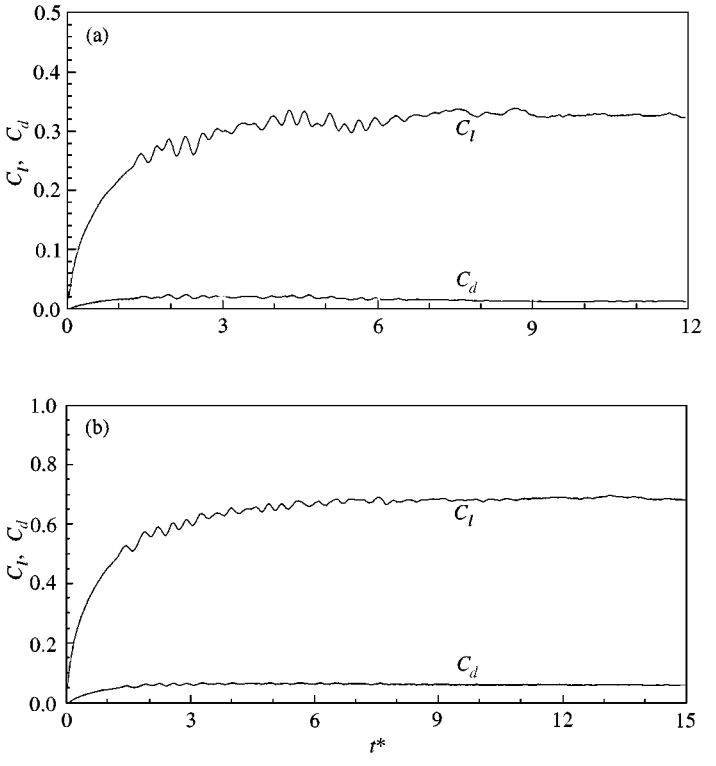

Figure 4. Time histories of the force coefficients for a fixed elliptic cylinder; $t/c = 0{\cdot}1$, Re = 3000: (a) $\bar{\alpha} = 5^\circ$, (b) $\bar{\alpha} = 10^\circ$.

the trailing-edge; see Figure 3(c-e). However, during the entire simulation the flow remains attached to the body surface, and no sign of flow separation is observed.

As shown in Figure 4, the drag coefficient (C_d) of the ellipse reaches steady state values of about 0·018 and 0·062 for $\bar{\alpha} = 5$ and 10°, and the lift coefficient (C_l) approaches values of 0·34 and 0·69, respectively. These simulations suggest $\partial C_l/\partial\alpha \approx 1{\cdot}28\pi$ for the attached flow over an ellipse with $t/c = 0{\cdot}1$.

When the angle of attack is increased to $\bar{\alpha} = 30^\circ$, however, significant changes occur in the flow field compared the previous case, as seen in Figure 5. Shortly after the impulsive start of the flow, at $t^* = 0{\cdot}5$, a leading-edge vortex starts to form (Figure 5(a)). As this vortex moves along the upper surface, a counter-rotating recirculation zone forms on the body-surface beneath the leading-edge vortex; see Figure 5(b,c). Starting at time $t^* = 3{\cdot}5$, the flow on the lower surface rolls up at the trailing-edge, and forms a vortex that interacts with the leading-edge vortex, as shown in Figure 5(d,e). Vortex shedding from the upper surface and the trailing-edge of the ellipse continues as the simulation progresses; see Figure 5(f,g).

The force coefficients for $\bar{\alpha} = 30^\circ$ demonstrate an unsteady behaviour, as shown in Figure 6. Both the lift and drag coefficients are considerably higher than for previous cases at lower angles of attack, especially the drag coefficient which increased dramatically, by one order of magnitude. Also shown in Figure 6 are the numerical results of Nair & Sengupta (1997) for the same conditions, where similar large values of force coefficients are predicted. However, the two sets of results show very different time histories. As mentioned previously, the present simulation shows that the flow separates from the ellipse shortly after the start of the flow, followed by a periodic vortex shedding from both the

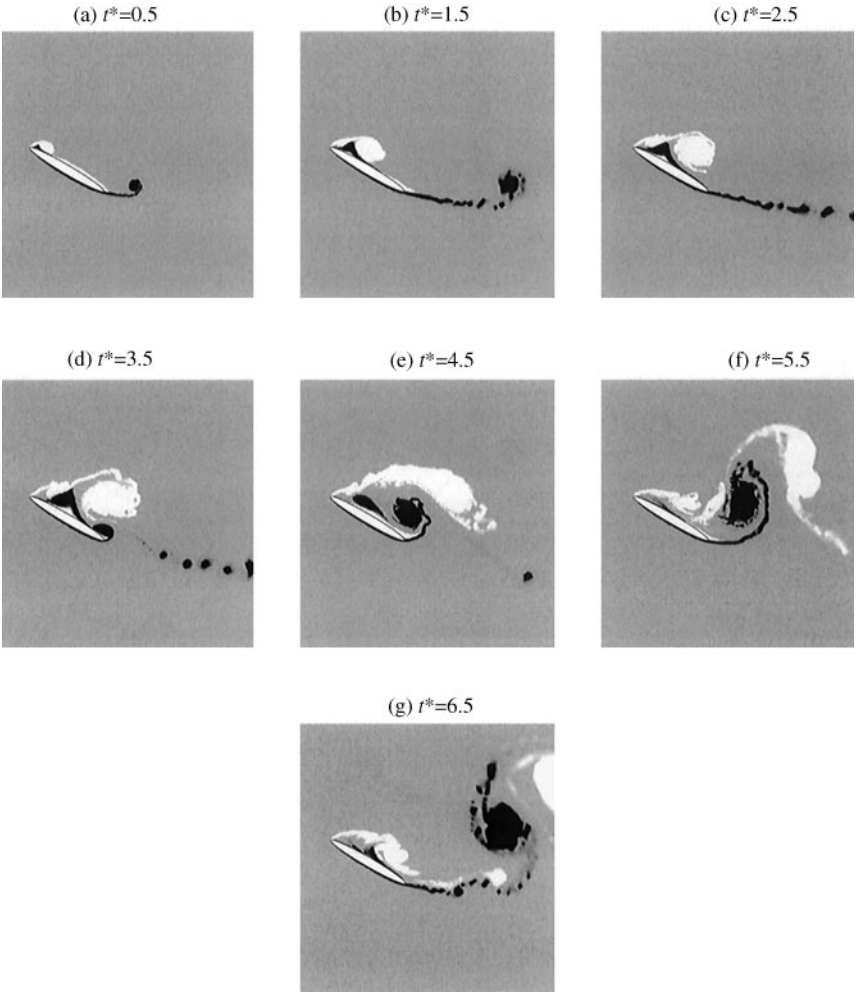

Figure 5. Vorticity contour plots at several instants of time for a fixed elliptic cylinder; $t/c = 0{\cdot}1$, $\tilde{\alpha} = 30^\circ$ and Re = 3000.

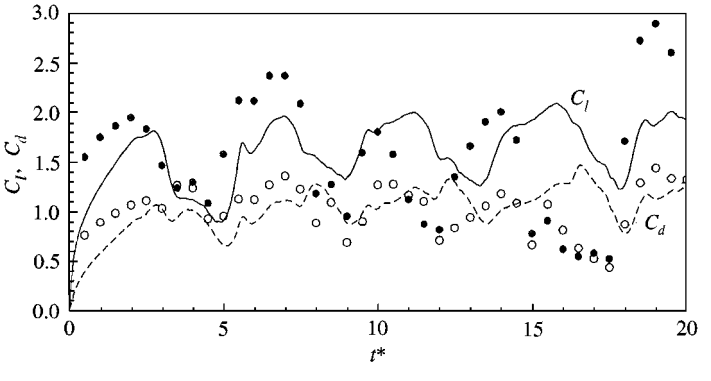

Figure 6. Time histories of the force coefficients C_l (—, ●) and C_d (- - -, ○) for a fixed elliptic cylinder; $t/c = 0{\cdot}1$, $\tilde{\alpha} = 30^\circ$ and Re = 3000; —, - - -: present study; ●, ○: numerical results due to Nair & Sengupta (1997).

upper surface and the trailing-edge of the ellipse. The force coefficients obtained from the present simulation demonstrate a periodic behaviour that is synchronized with the flow development and vortex shedding. This is not observed in the numerical results of Nair & Sengupt (1997), which do not seem to have reached a periodic behaviour by $t^* = 20$.

In the following, the pitching oscillations of an ellipse in a steady cross-flow are considered, and the effects of different parameters on the flow field are investigated.

4.1. Effect of Reduced Frequency

Computational results for the first two cycles of oscillation are presented in Figure 7, in terms of the vorticity contour plots, for a 10% thick ellipse oscillating with $f^* = 0{\cdot}2$. Results are shown at different instants of time up to $t^* = 10$. Also indicated for each part of the figure is the ratio t^*/T^*, where T^* is the period of the forced oscillation. Figure 7(a) shows that the flow remains attached to the airfoil up to $t^* = 0{\cdot}5$ after the impulsive start of the flow. However, at $t^* = 1{\cdot}0$ (Figure 7(b)) the first signs of a separated flow appear near the leading-edge. This separation bubble develops into a leading-edge vortex, that grows in both size and strength as the body reaches its maximum angle of incidence (Figure 7(c)). Meanwhile, a chain of small and opposite-sense vortices are continuously shed from the trailing-edge.

In the downstroke half of the first cycle of oscillation the large-scale leading-edge vortex continues to slowly detach from the airfoil surface and convects into the wake, while two smaller vortices develop at the leading-edge; see Figure 7(d,e). At the same time the trailing-edge continues to shed vortices. During the second cycle of oscillation, shown in Figure 7(f–j), a process of vortex shedding from the leading- and trailing-edges of the ellipse, similar to that in the first oscillation cycle, is observed. This is readily seen by comparing parts (c) to (e) of Figure 7, which are for the first cycle of oscillation, with parts (h)–(j), which are at exactly the same point in the second cycle of oscillation. Furthermore, a comparison of this flow field with that of a stationary ellipse (shown in Figure 5) suggests that the wake structure for this low-frequency pitching ellipse is not different fundamentally from that of a stationary ellipse at high angles of attack. However, during the upstroke, the upward motion of the leading-edge delays the flow separation and favours a more stable flow regime near the leading-edge. Furthermore, the downward motion of the leading-edge promotes separation of the main leading-edge vortex, and also induces the formation of smaller-scale leading-edge vortices. During the same period, the upward motion of the trailing-edge generates a string of negative-signed vortices in the wake.

Shown in Figure 8 are streamline sketches derived from visualization experiments on the same ellipse and for the same conditions as the present case, taken from Ohmi *et al.* (1990). The experiment was performed for two oscillation cycles of the airfoil. However, it was reported that the flow evolution of the second cycle was not very different from that of the first cycle, and that there were hardly any specific phenomena observable only in the second cycle. These experimental streamlines should be compared with those obtained numerically, shown in Figure 9. The agreement between the two sets of streamlines is very good for times up to $t^* = 3{\cdot}0$. In particular, the location and size of the leading- and trailing-edge vortices obtained from the numerical simulation are predicted very closely to the experimental visualization results. At $t^* = 3{\cdot}5$ the location of the large-scale leading-edge vortex is predicted somewhat off-course compared to the experiments, and the differences between the two flow fields continue to grow afterwards. However, during the entire simulation, the overall structure of the wake is predicted reasonably close to that seen in the experimental results.

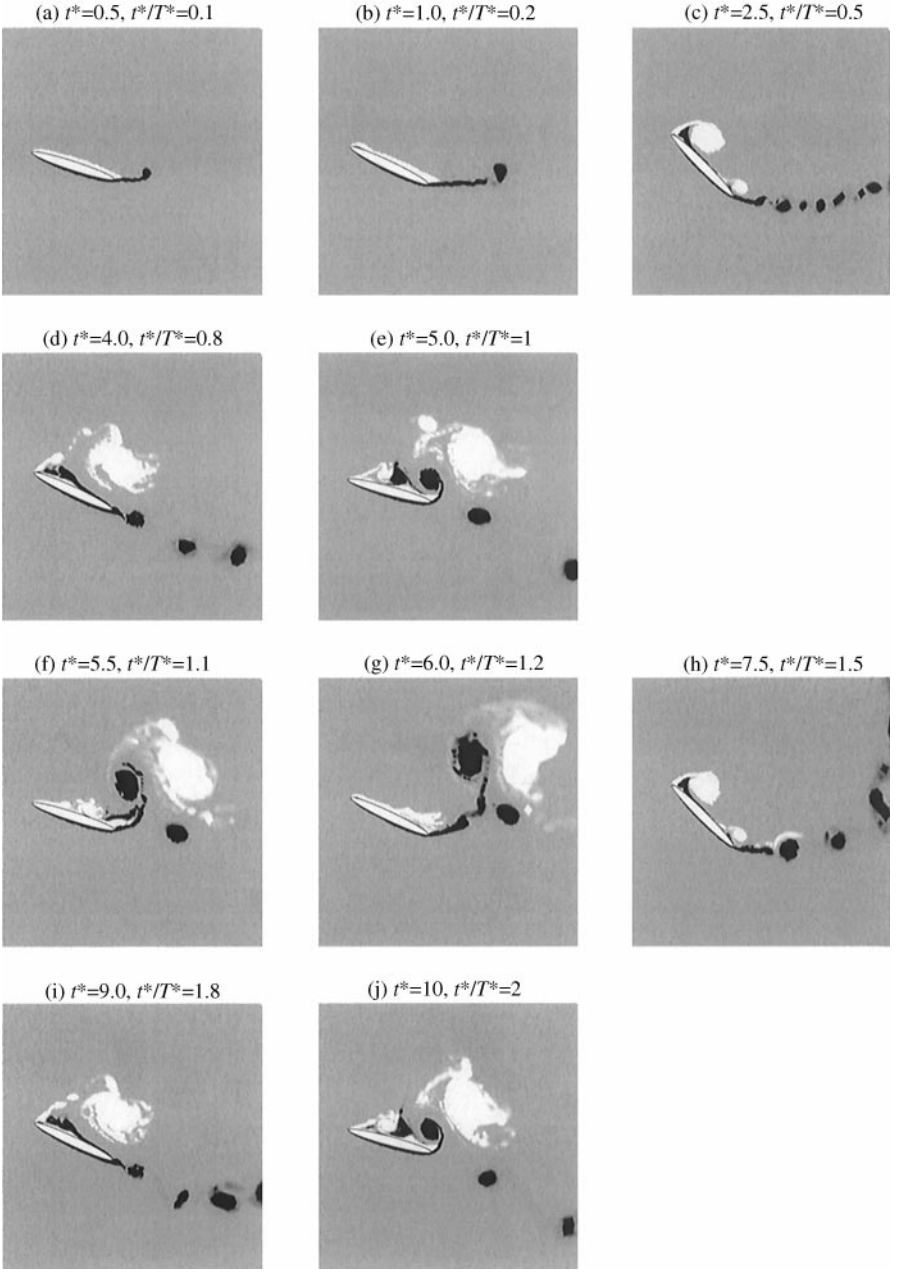

Figure 7. Vorticity contour plots at several instants of time for a pitching elliptic cylinder; $t/c = 0{\cdot}1$, $f^* = 0{\cdot}2$, $\Delta\alpha = 15^\circ$, $\bar{\alpha} = 30^\circ$, $\alpha_0 = 15^\circ$, rotation axis at $c/2$ and $\mathrm{Re} = 3000$.

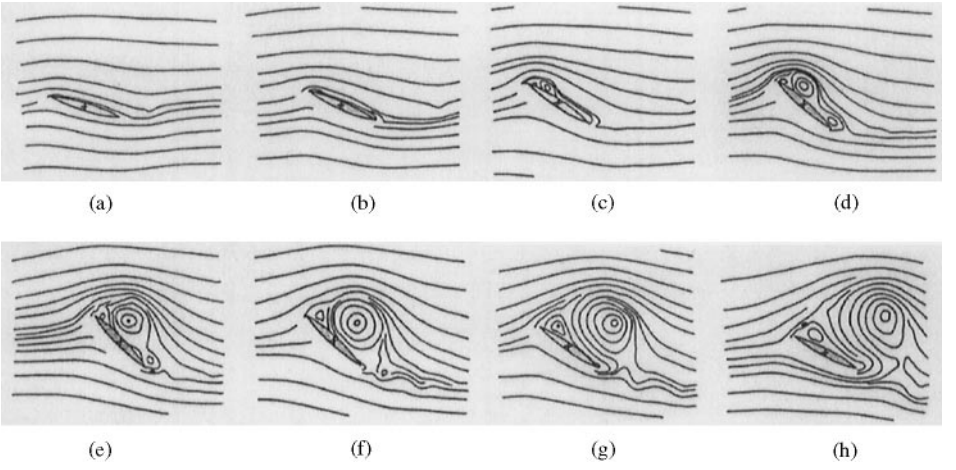

Figure 8. Experimental streamline plots for an ellipse; $t/c = 0{\cdot}1$, $f^* = 0{\cdot}2$, Re = 3000, $\bar{\alpha} = 30^\circ$, $\Delta\alpha = 15^\circ$ and $\alpha_0 = 15^\circ$ [taken from Ohmi *et al.* (1990)]: (a) $t^* = 0{\cdot}5$, (b) $t^* = 1{\cdot}0$, (c) $t^* = 1{\cdot}5$, (d) $t^* = 2{\cdot}0$, (e) $t^* = 2{\cdot}5$, (f) $t^* = 3{\cdot}0$, (g) $t^* = 3{\cdot}5$, (h) $t^* = 4{\cdot}0$.

Increasing the nondimensional oscillation frequency to $f^* = 1{\cdot}0$ produces a much more complex flow, as shown in Figure 10 for five complete cycles of oscillation. By the end of the first half-cycle of oscillation the starting vortex has already been released from the trailing-edge, and a separation bubble is forming at the leading-edge, as seen in Figure 10(a). At the end of the first cycle, Figure 10(b), a leading-edge vortex has completely formed, and a small-scale vortex has also formed at the trailing-edge during the downstroke. In the next oscillation cycle a trailing-edge vortex is formed during the upstroke, and a leading-edge vortex, with opposite sense, is formed during the downstroke; see Figure 10(c,d). In the third oscillation cycle the presence of the two (merging) leading-edge vortices in the vicinity of the trailing-edge suppresses the formation of a new trailing-edge vortex; this can be seen in Figure 10(e,f). In the following cycles a new vortex is formed at the leading-edge during every downstroke, while only a single trailing-edge vortex manages to form, as seen in Figure 10(g–j).

It is observed that the periodic formation of both the large- and small-scale vortices are controlled by the rotational motion of the leading- and trailing-edges at this higher frequency, unlike in the previous case with a lower frequency. Furthermore, due to the shorter oscillation period, the leading-edge vortices are not convected sufficiently far over the upper surface before the next one is formed at the leading-edge; hence, the number of vortices on the upper surface increases with time. On the other hand, the trailing-edge maintains its periodic shedding of vortices, thus pushing the leading-edge vortices away from the trailing-edge. This causes the vortices developed at the leading-edge to be shed from the upper surface rather than from the trailing-edge. This, in turn, produces a different type of wake, where two streams of vortices are shed almost in parallel to each other from the two edges.

The time histories of the force coefficients for $f^* = 1{\cdot}0$ are shown in Figure 11 for times up to $t^* = 13$. The lift coefficient reaches an almost periodic steady state after the end of the 4th oscillation cycle, with a time period of about three times the oscillation period of the airfoil. During one period of its fluctuation, the lift coefficient has maximum and minimum values of around 1·6 and 0·65, respectively. Its mean value, excluding the initial transient response during $t^* \leq 4$, is about 1. The drag coefficient has a dominant period equal to that of the airfoil oscillation; however, similar to the lift coefficient, its overall cyclic period is about

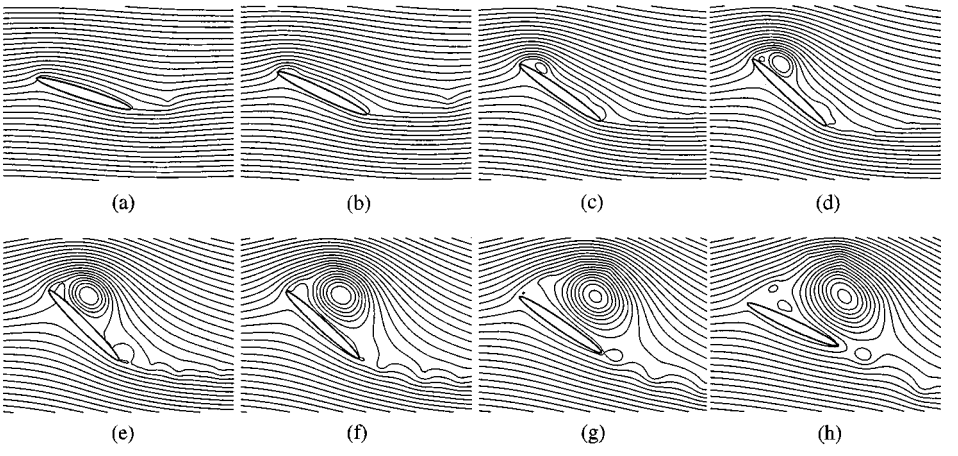

Figure 9. Numerical streamline plots for an ellipse; $t/c = 0{\cdot}1$, $f^* = 0{\cdot}2$, Re = 3000, $\bar{\alpha} = 30^\circ$, $\Delta\alpha = 15^\circ$ and $\alpha_0 = 15^\circ$: (a) $t^* = 0{\cdot}5$, (b) $t^* = 1{\cdot}0$, (c) $t^* = 1{\cdot}5$, (d) $t^* = 2{\cdot}0$, (e) $t^* = 2{\cdot}5$, (f) $t^* = 3{\cdot}0$, (g) $t^* = 3{\cdot}5$, (h) $t^* = 4{\cdot}0$.

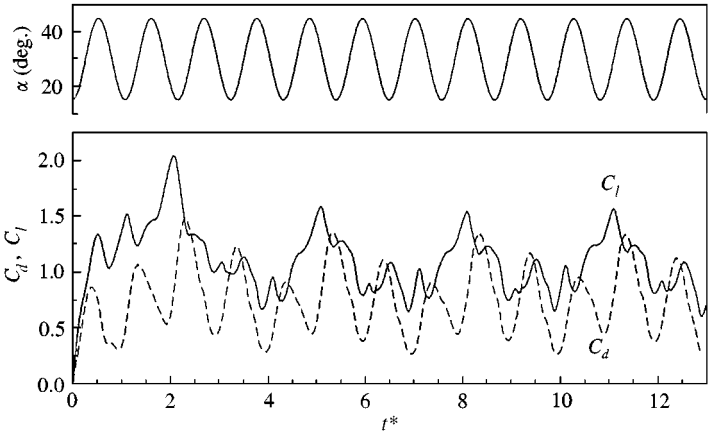

Figure 11. Time histories of the force coefficients for a pitching elliptic cylinder; $t/c = 0{\cdot}1$, $f^* = 1{\cdot}0$, $\Delta\alpha = 15^\circ$, $\bar{\alpha} = 30^\circ$, $\alpha_0 = 15^\circ$, rotation axis at $c/2$ and Re = 3000.

three times the airfoil oscillation period. This effect can be observed by comparing the drag coefficient response for $4 \leq t^* \leq 7$ with those for $7 \leq t^* \leq 10$ and $10 \leq t^* \leq 13$. The maximum and minimum values for the drag coefficient in one period of its fluctuation are 1·36 and 0·27, respectively. Also, the mean value of the drag coefficient, excluding the transient response, is about 0·75.

Increasing the frequency to $f^* = 2{\cdot}0$ produces the results presented in Figure 12, where 10 oscillation cycles are completed during the $t^* = 5{\cdot}0$ simulation time. Each part of the figure shows the flow field at the end of either a downstroke or an upstroke during the last five cycles of oscillation. Figure 12(a–d) shows that during each oscillation cycle two counter-rotating vortices are generated at the trailing-edge, and a positive vortex is formed at the leading-edge. However, the two counter-rotating vortices from the trailing-edge diffuse into each other as they move downstream.

As time increases, the formation of vortices from the trailing-edge continues almost regularly up to the 8th oscillation cycle [as seen in Figure 12(b–f)], while the leading-edge

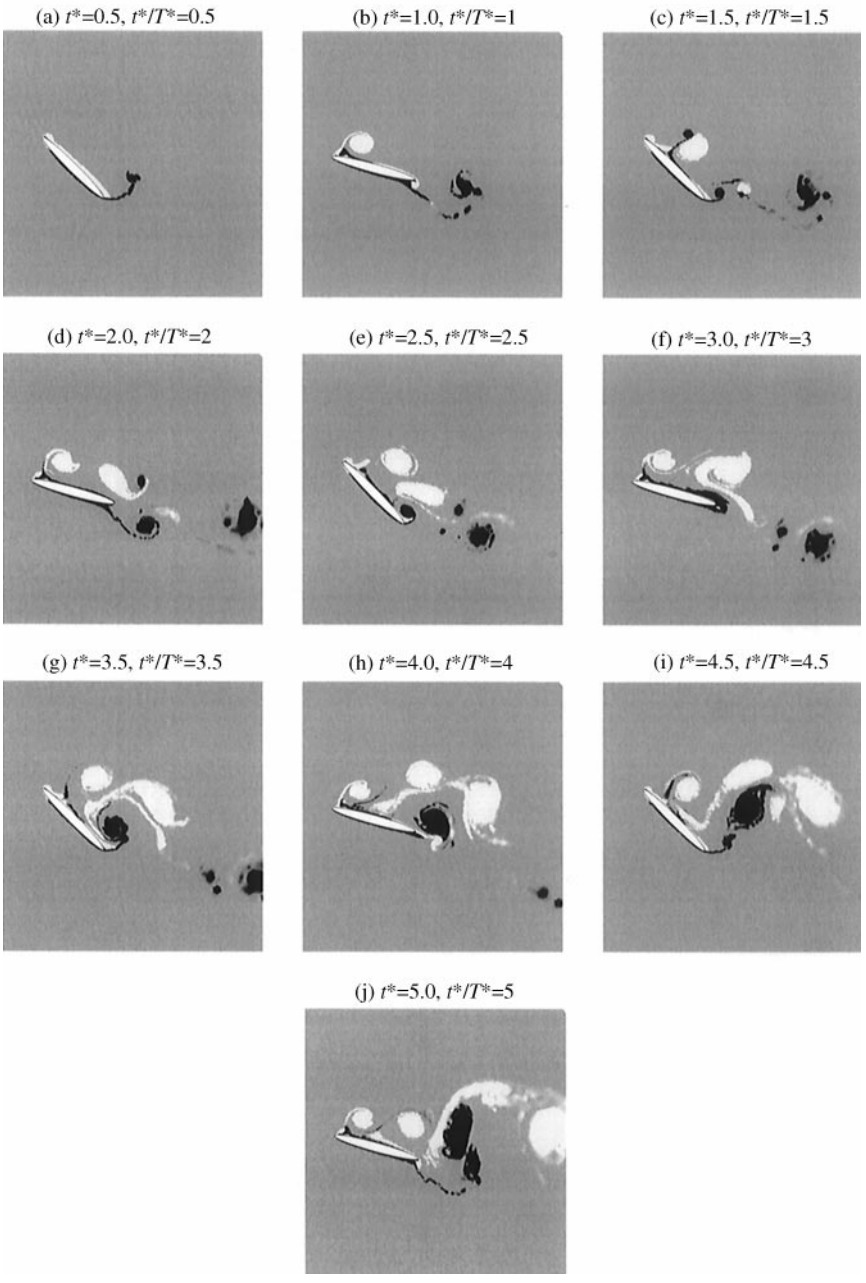

Figure 10. Vorticity contour plots at several instants of time for a pitching elliptic cylinder; $t/c = 0{\cdot}1$, $f^* = 1{\cdot}0$, $\Delta\alpha = 15^\circ$, $\bar{\alpha} = 30^\circ$, $\alpha_0 = 15^\circ$, rotation axis at $c/2$ and $\mathrm{Re} = 3000$.

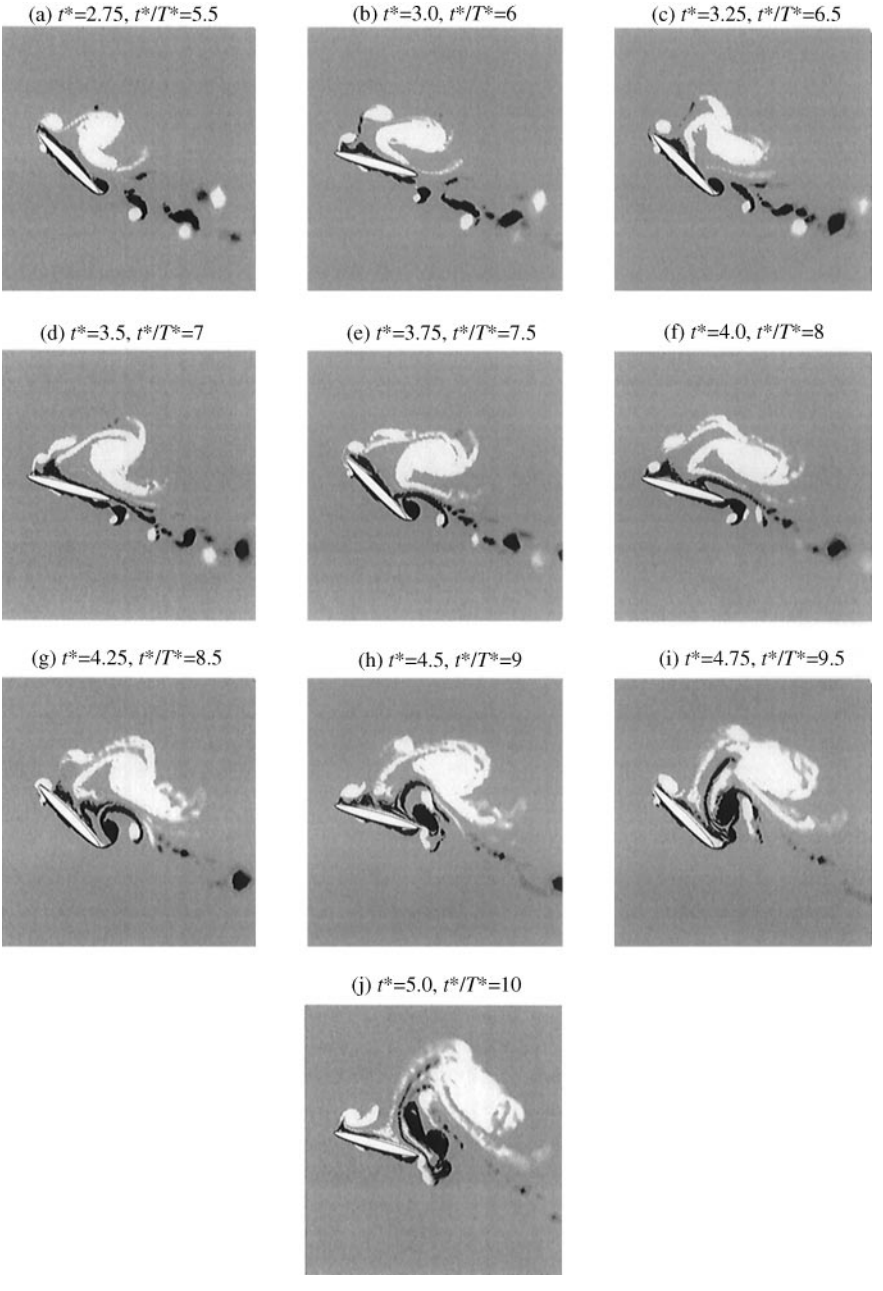

Figure 12. Vorticity contour plots at several instants of time for a pitching elliptic cylinder; $t/c = 0{\cdot}1$, $f^* = 2{\cdot}0$, $\Delta\alpha = 15^\circ$, $\bar{\alpha} = 30^\circ$, $\alpha_0 = 15^\circ$, rotation axis at $c/2$ and $\mathrm{Re} = 3000$.

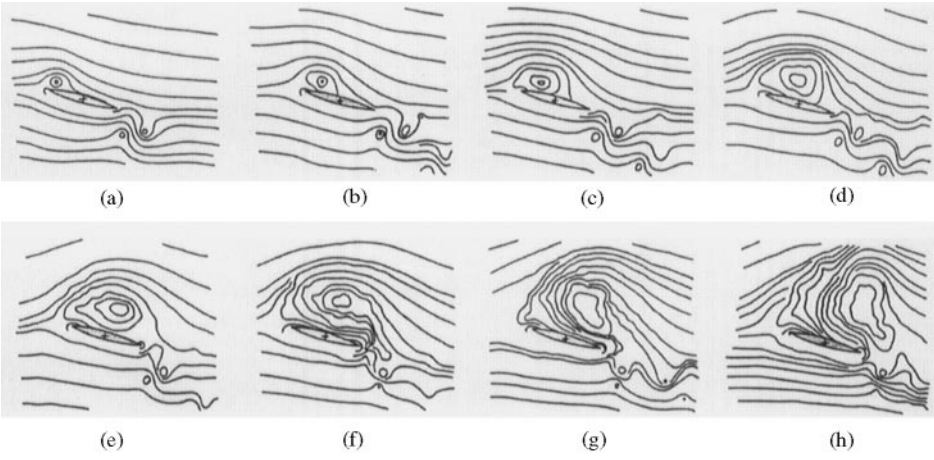

Figure 13. Experimental streamline plots for an ellipse; $t/c = 0{\cdot}1$, $f^* = 2{\cdot}0$, Re = 3000, $\bar{\alpha} = 30^\circ$, $\Delta\alpha = 15^\circ$ and $\alpha_0 = 15^\circ$ [taken from Ohmi *et al.* (1990)]: (a) $t^* = 0{\cdot}5$, (b) $t^* = 1{\cdot}0$, (c) $t^* = 1{\cdot}5$, (d) $t^* = 2{\cdot}0$, (e) $t^* = 2{\cdot}5$, (f) $t^* = 3{\cdot}0$, (g) $t^* = 3{\cdot}5$, (h) $t^* = 4{\cdot}0$.

vortices continue to interact with each other, and form a large-scale vortex on the upper surface of the body. The strength of this large-scale leading-edge vortex is large enough, so that when it moves close to the trailing edge it suppresses the regular formation of the trailing-edge vortices; see Figure 12(f–j). In the last two oscillation cycles, shown in Figure 12(f–j), a vortex forms at the leading-edge, while the vortices from the trailing-edge are trapped by the large-scale leading-edge vortex.

In this case, similar to the previous case with $f^* = 1$, the periodic formation of vortices and the wake structure are dominated by the pitching motion of the airfoil. At this higher frequency, however, alternate vortices are generated at the trailing-edge during both the upstroke and downstroke. Furthermore, the formation frequency of small-scale leading-edge vortices is so high that they hardly move before the next one coalesces with them, forming a single large-scale leading-edge vortex during $t^* \leq 5$.

The experimental flow visualization results for this case ($f^* = 2$), taken from Ohmi *et al.* (1990), are shown in Figure 13 and the corresponding numerical streamline plots are shown in Figure 14. Each part of the figures shows the flow field at the end of an oscillation cycle. As seen in parts (a) and (b) of the figures, the numerical simulation predicts the flow field quite accurately up to the end of the second cycle. At the end of the third oscillation cycle, part (c) of the figures, the vortex on the airfoil surface is predicted to be a little flatter than that seen in the flow visualization results; but the size and location of the vortices in the flow fields are still very comparable. As time increases, the differences between the simulation and experiments grow, however, qualitatively the comparison remains reasonably good. For example, at the end of the 8th oscillation cycle the numerical simulation predicts a large vortex structure on the airfoil surface, and a small vortex in the wake just below the trailing-edge (see Figure 14(b)); this is very similar to the corresponding visualization results, shown in Figure 13(h).

4.2. Effect of Mean Angle of Attack

The results of Figure 15 show the vorticity contours when the mean angle of attack is set at $\bar{\alpha} = 0^\circ$, and the body oscillates between $+15^\circ$ and -15°, starting from the positive angle, with a reduced frequency of $f^* = 1{\cdot}0$. These conditions are identical to those for the results

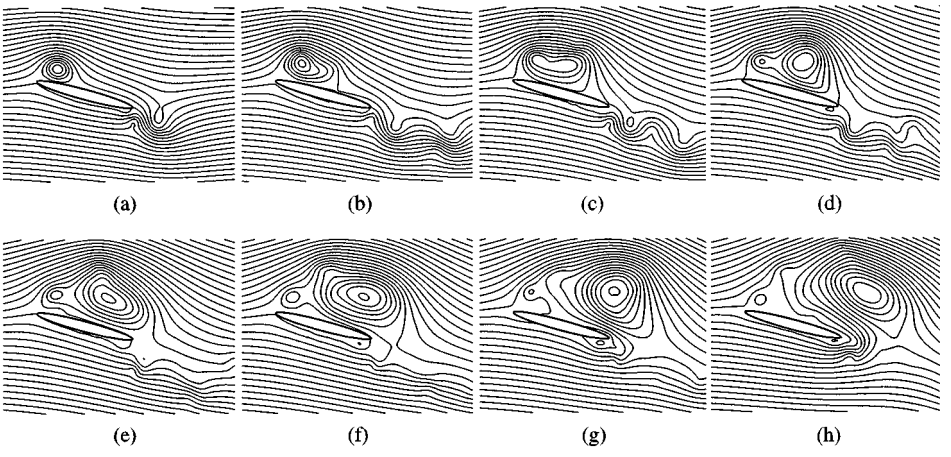

Figure 14. Numerical streamline plots for an ellipse; $t/c = 0{\cdot}1$, $f^* = 2{\cdot}0$, Re = 3000, $\bar{\alpha} = 30^\circ$, $\Delta\alpha = 15^\circ$ and $\alpha_0 = 15^\circ$: (a) $t^* = 0{\cdot}5$, (b) $t^* = 1{\cdot}0$, (c) $t^* = 1{\cdot}5$, (d) $t^* = 2{\cdot}0$, (e) $t^* = 2{\cdot}5$, (f) $t^* = 3{\cdot}0$, (g) $t^* = 3{\cdot}5$, (h) $t^* = 4{\cdot}0$.

shown in Figure 10, except for the mean incidence. The flow field at the end of the first downstroke, when $\alpha = -15^\circ$, is shown in Figure 15(a), indicating that the starting vortex has been released, and two co-rotating vortices have formed at the leading- and trailing-edges. In the upstroke of the same cycle, the leading-edge vortex travels along the upper surface, and a counter-rotating vortex forms on the lower side of the leading-edge; meanwhile, a new vortex forms at the trailing-edge from its lower side, see Figure 15(b). Figure 15(c) shows the flow field at the end of the 2nd downstroke, where two co-rotating vortices have formed on the upper surface at the leading- and trailing-edges.

The formation of a pair of co-rotating vortices from the lower side of the leading- and trailing-edges during every upstroke, and another pair of vortices, with opposite sense, from the upper side during every downstroke continues in the following cycles, as seen in Figure 15(e–j). The vortices generated at the leading-edge travel along the surface of the body, and are shed from the trailing-edge one oscillation cycle later. However, before the vortex can be completely shed, the pitching direction of the body reverses, and the remainder of the vortex is discharged from the trailing-edge 3/4 of a cycle later when the body is almost at $\alpha = 0^\circ$. Hence, there is only a 1/4 of an oscillation cycle time difference between the shedding of a vortex and the next co-rotating vortex from the same side of the body, as seen in Figure 15(g–i). This regular vortex shedding from the trailing-edge forms an organized vortex street in the wake of the body. The vortex shedding is fully controlled by the oscillation in this case, as leading- and trailing-edge vortices are regularly shed during every cycle of oscillation.

The wake structure for this angle of attack is fundamentally different from that presented in previous cases. However, it should be noted that the airfoil oscillates between moderate angles of attack in this case, as opposed to the previous cases where very high angles of attack were considered. Nevertheless, this demonstrates that the mean angle of attack has a major effect on the flow field, even though other parameters, such as the angular amplitude of oscillation, also affect the flow field.

The time histories of the force coefficients for $\bar{\alpha} = 0^\circ$ are shown in Figure 16. The drag coefficient shows a well-defined periodic behaviour immediately after the impulsive start of the flow, with a frequency equal to twice the oscillation frequency. The lift coefficient also shows a periodic behaviour; however, its frequency is equal to that of the forced oscillation.

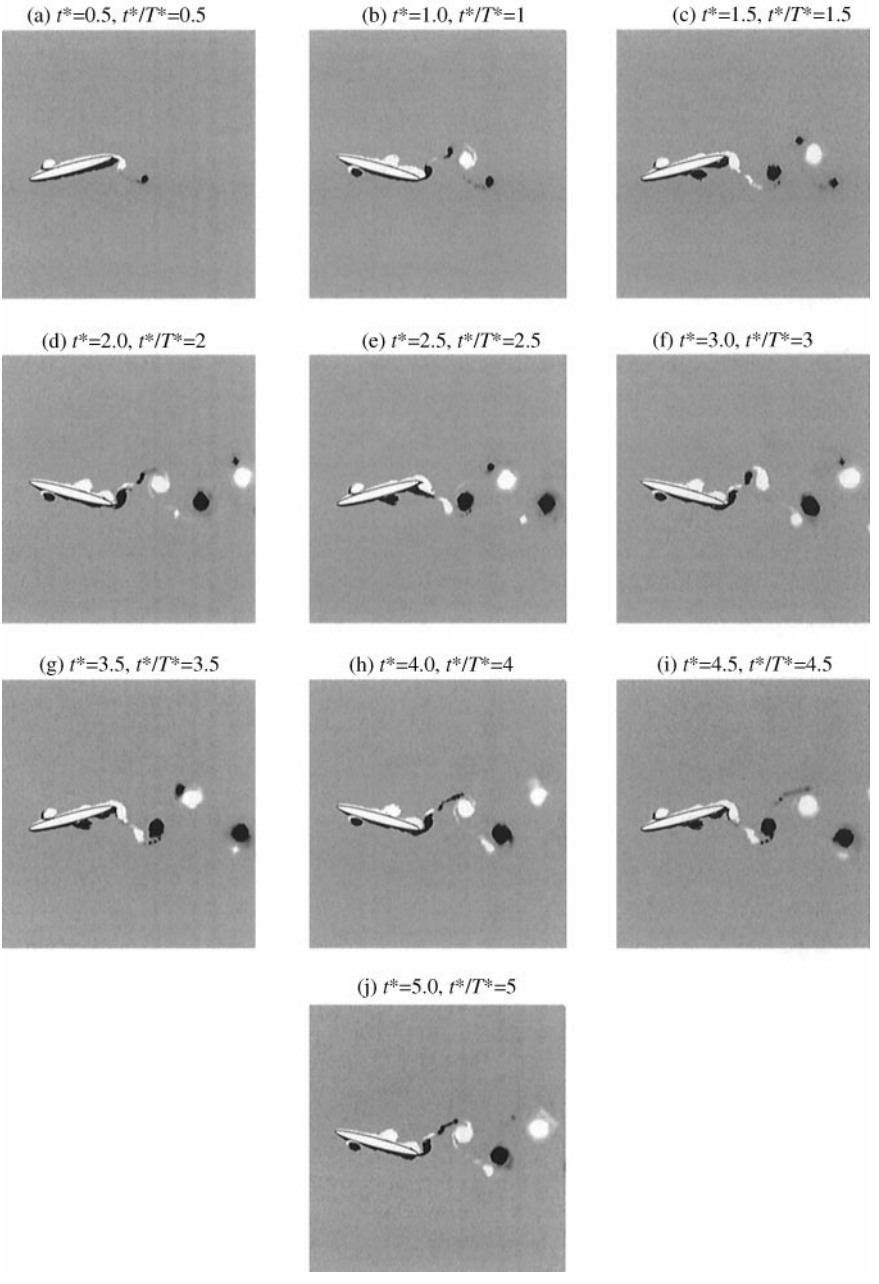

Figure 15. Vorticity contour plots at several instants of time for a pitching elliptic cylinder; $t/c = 0{\cdot}1$, $f^* = 1{\cdot}0$, $\Delta\alpha = 15^\circ$, $\bar{\alpha} = 0^\circ$, $\alpha_0 = 15^\circ$, rotation axis at $c/2$ and Re = 3000.

Furthermore, the lift coefficient lacks the (almost) sinusoidal profile seen in the drag coefficient response.

4.3. Effect of Pitch-axis Location

In all of the previous examples the pitch-axis was located at the mid-chord. Moving the pitch-axis to the quarter-chord point produces the vorticity contours shown in Figure 17.

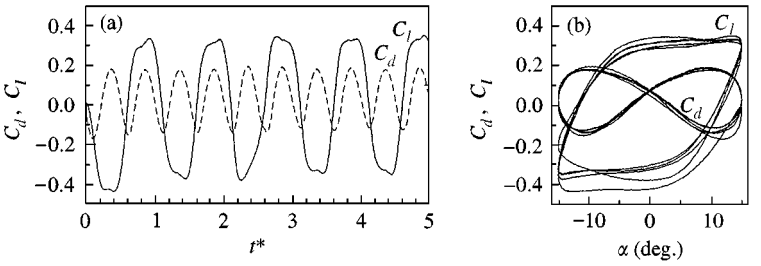

Figure 16. The force coefficients for a pitching elliptic cylinder; $t/c = 0{\cdot}1$, $f^* = 1{\cdot}0$, $\Delta\alpha = 15^\circ$, $\bar{\alpha} = 0^\circ$, $\alpha_0 = 15^\circ$, rotation axis at $c/2$ and $\mathrm{Re} = 3000$: (a) time histories, (b) traces versus angle of attack.

At $t^* = 0{\cdot}5$, Figure 17(a), the flow field is very similar to that with pitch-axis at the mid-chord at the same instant of time, shown in Figure 10(a), except that both the leading-edge separation bubble and the starting vortex seem to be stronger in the present case. This is due to a lower rate of ascent of the leading-edge, and a higher rate of descent of the trailing-edge in the present case compared with the simulations presented in Figure 10. Note that an upward motion of the leading-edge favours a more stable flow at high angles of attack, and delays flow separation.

A leading-edge vortex is formed during every downstroke, as seen in Figure 17(b,d,f,h,j). However, the leading-edge vortices travel a longer distance on the upper surface during the next upstroke than when the pitch-axis is at the mid-chord (cf. Figures 10(c) and 17(c)); this is due to the higher suction caused by the rapidly descending trailing-edge when the pitch-axis is at the quarter-chord. Moreover, not only trailing-edge vortices are formed during every upstroke, but also smaller-scale vortices are formed during some downstrokes on the lower surface near the trailing-edge, see Figure 17(b,d,h).

The main effect of moving the pitch-axis to the quarter-chord is that both the leading- and trailing-edge vortices are stronger than those with the pitch-axis at the mid-chord. Also, coalescence of the leading-edge vortices occurs earlier in this case due to higher travelling speed of the vortices on the upper surface. This changes the details of the flow field, and leads to a more unstable and complex wake structure. However, the overall features of the wake pattern are very similar for the two positions of the pitch-axis.

4.4. Effect of Thickness Ratio

Increasing the thickness ratio to $t/c = 0{\cdot}25$ from $t/c = 0{\cdot}1$, as considered in the previous cases, produces results as shown in Figure 18. A leading-edge vortex is formed during every downstroke, Figure 18(b,d,f,h,j). However, trailing-edge vortices are not formed in as regular a manner as with $t/c = 0{\cdot}1$. The formation of a trailing-edge vortex can be seen during the 2nd oscillation cycle, Figure 18(c,d). But, the next trailing-edge vortex is formed during the period of $2{\cdot}5 < t^* < 3{\cdot}5$, as shown in Figure 18(e–g). The slow convection of this vortex in the wake can be followed in the rest of the simulation, Figure 18(h–j). It is observed that in this case pairs of leading-edge vortices merge and form a large-scale vortex that dominates the near-wake for some time.

The formation of leading-edge vortices for $t/c = 0{\cdot}25$ is just as regular as when $t/c = 0{\cdot}1$, i.e., one during every downstroke. However, trailing-edge vortices are *not* formed as regularly as in the previous cases. This phenomenon can be attributed to the lower curvature of the trailing-edge when $t/c = 0{\cdot}25$. Due to the lower curvature, the rolling up of the flow on the lower surface of the body during the upstrokes is not as intense as for the thinner ellipse;

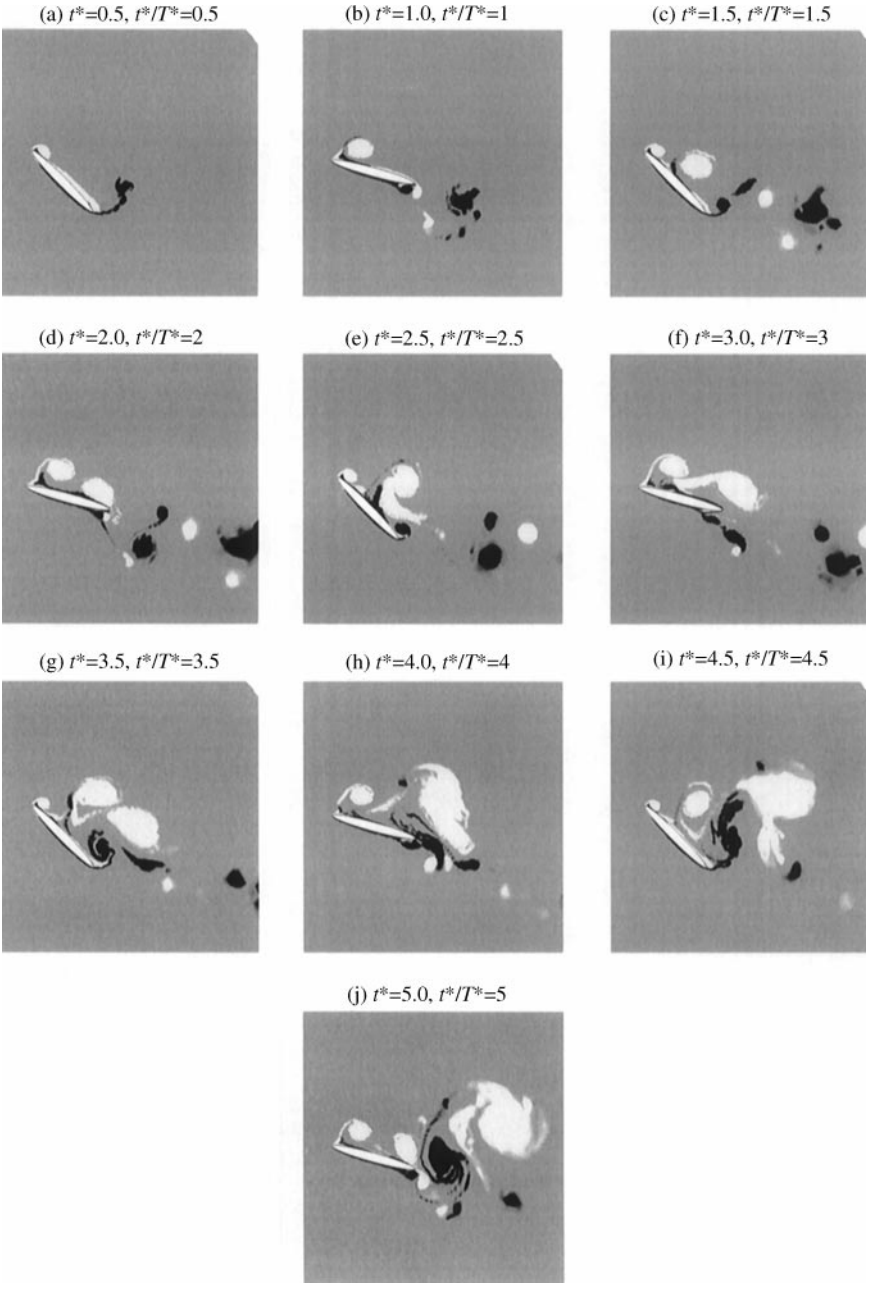

Figure 17. Vorticity contour plots at several instants of time for a pitching elliptic cylinder; $t/c = 0{\cdot}1$, $f^* = 1{\cdot}0$, $\Delta\alpha = 15^\circ$, $\bar{\alpha} = 30^\circ$, $\alpha_0 = 15^\circ$, rotation axis at $c/4$ and $\mathrm{Re} = 3000$.

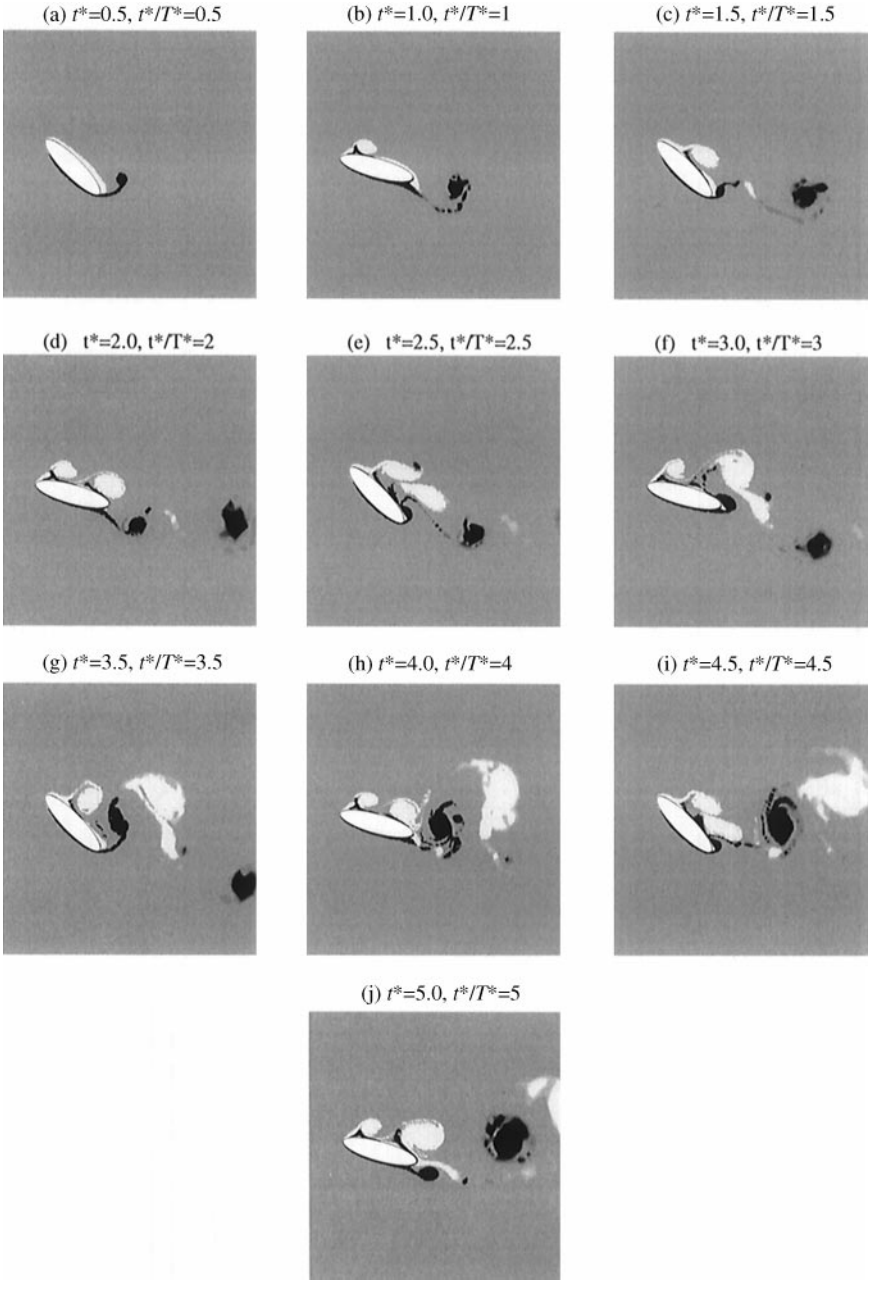

Figure 18. Vorticity contour plots at several instants of time for a pitching elliptic cylinder; $t/c = 0{\cdot}25$, $f^* = 1{\cdot}0$, $\Delta\alpha = 15^\circ$, $\bar{\alpha} = 30^\circ$, $\alpha_0 = 15^\circ$, rotation axis at $c/2$ and Re = 3000.

hence, there is a weaker formation of the trailing-edge vortices. The wake structure for $t/c = 0{\cdot}25$ is less complex and more organized than for the thinner ellipse. It is mainly composed of a large-scale leading-edge vortex (formed by the coalescence of two original leading-edge vortices), and the trailing-edge vortices that are shed once during every two oscillation cycles. Hence, there is a well-balanced vortex street downstream of the ellipse.

5. CONCLUSIONS

The flow field around elliptic airfoils in pitching oscillations has been simulated, and the effects of several parameters on the flow structure examined. These parameters included the frequency of oscillation, mean angle of attack, location of the pitch-axis and the thickness ratio.

It was observed that the frequency of oscillation has a significant effect on the flow structure. At the lowest reduced frequency considered, $f^* = 0{\cdot}2$, the wake structure did not show any significat difference compared to that for a stationary ellipse at high angles of attack. The minor differences noted were due to the ascending motion of the leading-edge which delayed the flow separation, and the periodic motion of the trailing-edge which caused the formation of trailing-edge vortices. At a higher reduced frequency of $f^* = 1{\cdot}0$, the periodic formation of both the leading- and trailing-edge vortices was controlled by the rotational motion of the airfoil. Also, because of the shedding of the leading-edge vortices from the upper surface (rather than the trailing-edge) a different type of wake structure was observed. At the highest reduced frequency considered in these simulations, $f^* = 2{\cdot}0$, the formation of vortices was controlled by the pitching oscillation of the airfoil, similar to the behaviour with $f^* = 1{\cdot}0$. Furthermore, in this case, alternate vortices were observed to form at the trailing-edge during both the upstroke and downstroke of the ellipse. The numerical results for these cases were in good agreement with corresponding experimental flow-visualization results.

It was observed that the mean angle of attack has a significant effect on both the vortex formation mode and the wake pattern. For example, with a mean angle of attack of $\bar{\alpha} = 0^\circ$ an organized vortex street was observed in the wake of the airfoil, as opposed to a wide, complex wake structure seen for the same pitching airfoil with $\bar{\alpha} = 30^\circ$. Well-defined periodic force coefficients were obtained with $\bar{\alpha} = 0^\circ$.

Moving the pitch-axis from the mid-chord to the quarter-chord caused the formation of stronger leading- and trailing-edge vortices, which lead to a more unsteady and complex wake structure. However, the fundamental characteristics of the flow field remained the same as those obtained with the pitching axis at the mid-chord.

The flow around a thicker ellipse with $t/c = 0{\cdot}25$, rather than with $t/c = 0{\cdot}1$, was also simulated. It was observed that, similar to previous cases, a leading-edge vortex was formed during every downstroke of the ellipse. However, trailing-edge vortices did not form as regularly as those over the thinner ellipse. This was attributed to the lower curvature at the trailing-edge of the thicker ellipse. As a result of the coalescence of every two leading-edge vortices, and the formation of trailing-edge vortices during every two cycles, a different type of wake pattern was observed in this case.

ACKNOWLEDGMENTS

The authors gratefully acknowledge the financial support from the Natural Sciences and Engineering Research Council of Canada (NSERC) and Les Fonds FCAR du Québec.

References

Akbari, M. H. 1999 Bluff-body flow simulations using vortex methods. Ph.D. thesis, McGill University, Montréal, Canada.

Akbari, M. H. & Price, S. J. 1997 Simulation of the incompressible viscous cross-flow around an oscillating circular cylinder via the random vortex method. *Proceedings of 4th International Symposium on Fluid-Sructure Interctions, Aeroelasticity, Flow-Induced Vibration and Noise* (eds M. P. Paidoussis *et al.*), AD-Vol. 531, pp. 21–32. New York: ASME.

Beale, J. T. & Majda, A. 1981 Rates of convergence for viscous splitting of the Navier-Stokes equations. *Mathematics of Computation* **37,** 243–259.

Chou, M-H. & Huang, W. 1996 Numerical study of high-Reynolds-number flow past a bluff object. *International Journal for Numerical Methods in Fluids* **23,** 711–732.

Chorin, A. J. 1973 Numerical study of slightly viscous flow. *Journal of Fluid Mechanics* **57,** 785–796.

Lugt, H. J. & Haussling, H. J. 1974 Laminar flow past an abruptly accelerated elliptic cylinder at 45° incidence. *Journal of Fluid Mechanics* **65,** 711–734.

Meneghini, J. R. & Bearman, P. W. 1993 Numerical simulation of high amplitude oscillatory-flow about a circular cylinder using a discrete vortex method. *AIAA Shear Flow Conference*, July 6–9, 1993, Orlando, FL, U.S.A. *AIAA paper* 93–3288.

Mittal, R. & Balachandar, S. 1996 Direct numerical simulation of flow past elliptic cylinders. *Journal of Computational Physics* **124,** 351–367.

Modi, V. J. & Dikshit, A. K. 1975 Near-wakes of elliptic cylinders in subcritical flow. *AIAA Journal* **13,** 490–497.

Modi, V. J. & Wiland, E. 1970 Unsteady aerodynamics of stationary elliptic cylinders in subcritical flow. *AIAA Journal* **8,** 1814–1821.

Nair, M. T. & Sengupta, T. K. 1996 Onset of asymmetry: flow past circular and elliptic cylinders. *International Journal for Numerical Methods in Fluids* **23,** 1327–1345.

Nair, M. T. & Sengupta, T. K. 1997 Unsteady flow past elliptic cylinders. *Journal of Fluids and Structures* **11,** 555–595.

Ohmi, K., Coutanceau, M., Phuoc loc, T. & Dulieu, A. 1990 Vortex formation around an oscillating and translating airfoil at large incidences. *Journal of Fluid Mechanics* **211,** 37–60·

Ota, T., Nishiyama, H. & Taoka, Y. 1985 Flow around an elliptic cylinder in the critical Reynolds number regime. *ASME Journal of Fluids Engineering* **109,** 149–155.

Smith, P. A. & Stansby, P. K. 1988 Impulsively started flow around a circular cylinder by the vortex method. *Journal of Fluid Mechanics* **194,** 45–77.

Swarztrauber, P. & Sweet, R. 1975 *Efficient FORTRAN Subprograms for the Solution of Elliptic Partial Differential Equations*. National Center for Atmospheric Research, Boulder, CO, U.S.A., NCAR-TN/IA-109.

Ying, L. A. 1990 Viscous splitting for the unbounded problem of the Navier-Stokes equations. *Mathematics of Computation* **55,** 89–113.